PNAS
www.pnas.org

Supplementary Information for

Structure of a Tc holotoxin pore provides insights into the translocation mechanism

Daniel Roderer[1], Oliver Hofnagel[1], Roland Benz[2], Stefan Raunser[1,*]

[1]Department of Structural Biochemistry, Max Planck Institute of Molecular Physiology, Otto-Hahn-Str. 11, 44227 Dortmund, Germany

[2]Department of Life Sciences and Chemistry, Jacobs University Bremen, Campusring 1, 28759 Bremen, Germany

[*]Correspondence to: stefan.raunser@mpi-dortmund.mpg.de

This PDF file includes:

Supplementary text
Figures S1 to S11
Legends for Movies S1 to S6
Tables S1 to S3
SI References

Other supplementary materials for this manuscript include the following:

Movies S1 to S6

www.pnas.org/cgi/doi/10.1073/pnas.1909821116

Supplementary Information Text

Methods

Protein production. *P. luminescens* TcdA1 (TcA) was expressed in *E. coli* BL21-CodonPlus (DE3)-RIPL in LB medium and purified as described previously (1). Fusion proteins *P. luminescens* TcdB2-TccC3 (TcB-TcC(WT)) and cleavage-deficient TcdB2-TccC3 variant D651A (TcB-TcC(D651A)) were also expressed in *E. coli* BL21-CodonPlus (DE3)-RIPL in LB medium and purified as described previously (2), as well as all TcB-TcC mutants. The nanodisc scaffold protein MSP1D1 was expressed and purified using pMSP1D1 (Addgene #20061) as described previously (3).

Holotoxin formation and nanodisc integration. TcdA1 and TcdB2-TccC3(WT) or TcdB2-TccC3(D651A) were mixed with a 1.5-fold excess of TcB-TcC over TcA pentamer and subsequently the excess of TcB-TcC was separated from the holotoxin by size exclusion chromatography (SEC) on a Superose 6 5/150 column (GE Life Science). For ABC(D651A), the holotoxin was concentrated to 1 mg/ml and mixed with a 12-fold molar excess of pre-formed MSP5ΔH5-POPC nanodiscs (Cube Biotech) in 20 mM Tris-HCl pH 8.0, 250 mM NaCl, followed by 1 h of incubation on ice. For ABC(WT), nanodiscs were pre-formed using MSP1D1 and POPC in a 1:55 molar ratio. The holotoxin was concentrated to 1.2 mg/ml and mixed with a 10-fold molar excess of nanodiscs in 20 mM Tris-HCl pH 8.0, 250 mM NaCl, followed by 1 h of incubation on ice. Subsequently, the holotoxin/nanodisc mixtures were dialyzed against 20 mM CAPS-NaOH pH 11.2, 250 mM NaCl for 2 days at 4 ºC. After dialysis, the holotoxin/nanodisc mixtures were subjected to SEC on a Superose 6 5/150 column equilibrated in 20 mM Tris-HCl pH 8.0, 250 mM NaCl, and the main peak containing ABC in nanodiscs was used for subsequent cryo-EM (SI Appendix, Fig. S1B,C).

Liposome overlay assay. TcA (1 mg/ml) was mixed with different lipid mixes dissolved in 5% β-D-octylglucoside (Anatrace) with a total lipid concentration of 5 mg/ml. We tested POPC, POPC + 20% liver PI, POPC + 20% POPG, POPC + 20% cholesterol, POPC + 20% sulfatide (porcine brain), DOPC, BPL and ECL. All lipids were purchased from Avanti Polar Lipids (Alabaster, AL 35007). After 1 h of incubation of TcA and lipids dissolved in OG at 4 ºC and pH 8, the mixtures were dialyzed against 20 mM CAPS-NaOH pH 11.2, 150 mM NaCl for 2 days at 4 ºC. Subsequently, the dialyzed proteoliposomes were mixed 1:1 with 60% glucose in dialysis buffer to 100 µl total volume, overlaid with 125 µL 25% glucose and 30 µL dialysis buffer and centrifuged at 175,000×g for 4 h at 4 ºC in a Beckman TLA 120.1 rotor. After centrifugation, the top and bottom fractions of the sucrose gradient were analyzed via SDS-PAGE and the respective TcA amounts were quantified via band densitometry.

Single channel conductance measurements. We measured the single channel conductance of TcA with different lipid compositions with black lipid membrane experiments. All lipids were obtained from Avanti Polar Lipids. The instrumentational setup consisted of a Teflon chamber with two compartments of 5 ml each which are connected by a small hole with a surface area of 0.4 mm^2. The membrane current was measured with a pair of Ag/AgCl electrodes with salt bridges. The electrodes were switched in series with a voltage source and homemade current amplifier on the basis of Burr Brown operational amplifier as described previously (1). Solutions of different lipids and lipid mixes (SI Appendix, Fig. S10) at 10 mg/ml total lipid concentration were prepared in 80% n-decane/20% butanol. The lipid solutions were “painted” across the hole, resulting in membrane formation. After the membrane turned black, 20 pM of TcA were added to the cis side (the black side) of the chamber. All measurements were performed with a membrane potential of 20 mV in 20 mM CAPS-NaOH pH 11, 1 M KCl.

Sample vitrification and cryo-EM data acquisition. For ABC(D651A), 2.4 µL of 0.12 mg/ml of the protein preparation were applied to glow-discharged holey carbon grids (Quantifoil, QF 2/1, 300 mesh) covered with a 2 nm carbon layer. 1.2 µL of 0.1% Tween-20 was added to the sample on the grid and blotting was performed immediately afterwards using a Cryoplunge3 (Cp3, Gatan) with

2.2 s blotting time at 20 ºC and 90% humidity. For ABC(WT), 2.8 µl of 0.10 mg/ml of the protein preparation were applied to glow-discharged holey carbon grids (Quantifoil, QF 2/1, 300 mesh) covered with a 2 nm carbon layer. Blotting was performed using a Vitrobot Mark IV (Thermo Fisher) with 2.5 s blotting time at 5 ºC and 100% humidity.
For ABC(D651A), two data sets were collected at a Cs-corrected Titan Krios EM (Thermo Fisher) equipped with an XFEG and a Falcon III direct electron detector operated in linear mode. Images were recorded using the automated acquisition program EPU (FEI) at a magnification of 59,000, corresponding to a pixel size of 1.11 Å/pixel on the specimen level. 12,040 movie-mode images were acquired in total in a defocus range of 1.2 to 2.6 µm. The total integration time was 1.5 s, partitioned into 40 movie frames with a total cumulative dose of ~ 100 $e^-/Å^2$. The data sets were merged for image processing.
For ABC(WT), one data set was collected at a Cs-corrected Titan Krios EM (Thermo Fisher) equipped with an XFEG and a K2 direct electron detector (Gatan). Images were recorded using the automated acquisition program EPU (FEI) at a magnification of 130,000, corresponding to a pixel size of 1.05 Å/pixel on the specimen level. 2,660 movie-mode images were acquired in a defocus range of 1.4 to 2.6 µm. Each movie comprised 40 frames acquired over 15 s with a total cumulative dose of ~ 61 $e^-/Å^2$.

Image processing
After initial screening, 8,903 integrated images were selected for further processing for ABC(D651A), and 2,053 integrated images were selected for further processing for ABC(WT). Movie frames were aligned, dose-corrected and averaged using MotionCor2 (4). CTF parameters were estimated using CTER (5), implemented in the SPHIRE software package (6). Outlier images were removed using the graphical CTF assessment tool in SPHIRE (6). For ABC(D651A), 2,400 particles were manually picked initially and 2D class averages used as an autopicking template were generated using ISAC (7) in SPHIRE. 619,594 particles were auto-picked from the images using Gautomatch (8) and extracted with a box size of 384 pixels. For ABC(WT), 390,353 particles were auto-picked using crYOLO (9) using a box size of 300 pixels. 269,142 particles were subsequently extracted using a box size of 420 pixels.
Reference-free 2D classification and cleaning of the dataset was performed with the iterative stable alignment and clustering approach ISAC in SPHIRE. ISAC was performed with a pixel size of 5.61 Å/pixel for ABC(D651A) and 5.80 Å/pixel for ABC(WT) on the particle level. The 'Beautifier' tool of SPHIRE was then applied to obtain refined and sharpened 2D class averages at the original pixel size, showing high-resolution features (SI Appendix, Fig. S2B, S5B). Only particles in ISAC classes showing a full holotoxin in the pore form were kept for 3D refinement, resulting in 337,823 particles for ABC(D651A) and 64,806 particles for ABC(WT), respectively.
We used the cryo-EM density map of the TcdA1 pore (EMD-4068 (2)), manually docked with a molecular map of TcB-TcC (pdb ID 4O9X) and filtered to 25 Å, as initial reference for 3D refinement. 3D refinement without imposing symmetry was performed in SPHIRE using MERIDIEN (6), using 7.5º initial angular sampling. 3D classification using SORT3D in SPHIRE, based on the final projection parameters of MERIDIEN, resulted in classes with different orientations of the asymmetric TcB-TcC cocoon in TcA. Therefore, one 3D class with well-defined density of TcB-TcC was locally refined, filtered to 5 Å and used as initial template in a new 3D refinement with 1.875º initial angular sampling. The resulting map provided a clearly defined density and only one distinct orientation of TcB-TcC for both ABC(D651A) and ABC(WT).
Post-processing of the final density maps obtained by 3D refinement was performed with the PostRefiner tool of SPHIRE using a soft Gaussian mask, resulting in final average resolutions of 3.9/3.4 Å for ABC(D651A) and 3.9/3.4 Å for ABC(WT), respectively, according to FSC 0.5/0.143 (SI Appendix, Fig. S2C, S5C). B-factors were -78.09 $Å^2$ for ABC(D651A) and -61.28 $Å^2$ for ABC(WT), respectively. Local FSC calculations were performed using the Local Resolution tool in SPHIRE. (SI Appendix, Fig. S2E, S5E). The density maps were filtered according to its local resolutions using the 3D Local Filter tool in SPHIRE.
To achieve a better local resolution in the TcB-TcC part of the map of ABC(D651A), we re-boxed particles after shifting the center of the map by 70 pixels to the center of the TcB-TcC cocoon using the final projection parameters of MERIDIEN (SI Appendix, Fig. S3A-C), and we ran MERIDIEN with the re-boxed particles. Post-processing, local FSC calculation and local filtering was performed

as described previously for the full map. The overall resolution of the obtained map is 4.2/3.7 Å according to FSC 0.5/0.143 (SI Appendix, Fig. S3E). 3D variability estimation was performed with sx3dvariability in SPHIRE. The input images were low-pass filtered to 25 Å and 20 images were used per projection.

Atomic model building and refinement

The cryo-EM density map of ABC(D651A) was used for atomic model building and refinement. Initially, models of TcdA1 in the pore form (pdb ID 5LKH and 5LKI) and TcB-TcC (pdb ID, 6H6F) were rigid-body fitted into the density map of the holotoxin. The chains of TcA, and the TcB-TcC fusion protein were individually fitted into the density map using Imodfit (10) to improve the initial fit of the model. Subsequently, we modeled the atomic structure of the holotoxin using an iterative combination of manual model building in Coot (11), Rosetta relaxation and Phenix real-space refinement (12) without imposing symmetry. Residues 1,382-1,491 of all TcA chains were removed, as the map showed insufficient density and resolution in that regions.

After initial modeling in the full holotoxin map, the model of TcB-TcC was further improved using the shifted map (SI Appendix, Fig. S6D,E), which allowed model building of the first residues of the ADP-ribosyltransferase of TccC3 after the mutated aspartyl protease cleavage site.

We created a fragment library of the ADP-ribosyltransferase (residues 679 – 960 of TcC) using the Robetta webserver (13) and attempted *de novo* building of the fragments into the density in the TcB channel using Rosetta. However, Rosetta *de novo* model building failed to create a reproducible model. We therefore manually built an unfolded Poly-Ala peptide in C-N translocation direction into the most well-defined density in the TcB channel. Afterwards, we added side chains at regions with sufficient density of possible peptide stretches close to the C-terminus of the ADP-ribosyltransferase and chose the best fitting model (SI Appendix, Fig. S7B).

The final models were validated by Rosetta relaxation against two independent half-maps (14), EMringer (15) and MolProbity (16) (SI Appendix, Table S1).

Cross-linking mass spectrometry

We incubated a 3 μM solution of TcB-TcC (WT or D651A) in 20 mM HEPES-NaOH pH 7.5, 150 mM NaCl with 3 mM disuccinimidyl dibutyric urea (DSBU, Thermo Fisher) for 30 min at 25 ºC. The cross-linking reaction was stopped by adding 100 mM Tris, followed by acetone precipitation. The precipitate was dissolved in 8 M urea, 1 mM DTT and alkylated with 5.5 mM iodacetamide for 30 min at 25 ºC. Afterwards, we diluted the solution 2-fold with 20 mM NH_4HCO_3 and digested with 1/50 molar ratio of endopeptidase LysC (Serva, MS grade) for 3 h at 25 ºC. Afterwards, we diluted again 2-fold with 20 mM NH_4HCO_3, added 1/100 molar amount of Trypsin (Sigma, MS grade) and continued proteolysis for 12 h at 25 ºC. Proteolysis was stopped by 0.1% trifluoracetic acid and the peptides were separated on a Superdex 30 increase 3.2-30 column (GE Life Science) equilibrated in 30% acetonitrile as described previously (17). Peptides eluting between retention volumes of 1.2 and 2.0 mL were collected in 100 µL fractions, evaporated in a speedvac and subsequently analyzed via LC-MS by the mass spectrometry facility of the Max Planck Institute of Molecular Physiology. Crosslinks were evaluated using MeroX (18) and visualized in xVis (19).

Bioinformatics tools.

Analysis of the TcB channel diameter and constrictions was performed with ChExVis (20) and visualized in UCSF Chimera (21). For visualization of the Coulomb potential, TcB was protonated using H++ (22) at pH 7.0 and an ionic strength of 150 mM. Homologs of TcdB2 were identified using Protein BLAST (23) and sequences of TcdB2 and 6 homologs were aligned in Clustal Omega (24). Sequence conservation of the hydrophobic and negatively charged patches in TcB and of the aspartyl protease cleavage site were analyzed with ConSurf (25) and visualized in UCSF Chimera.

Supplementary Figures

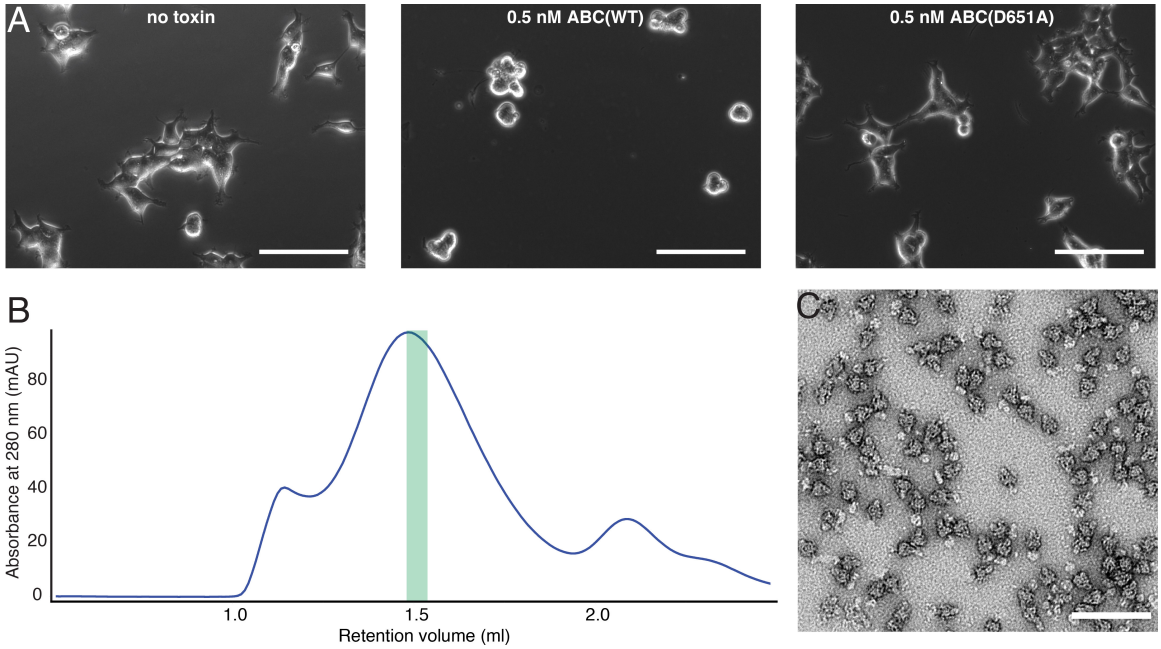

Fig. S1. Comparison of toxicity of ABC(WT) and ABC(D651A) and preparation of ABC(D651A) in nanodiscs.

A: Intoxication of HEK 293T cells with ABC(WT) and ABC(D651A). 2×10^4 cells in DMEM/F12 medium were incubated with PBS or 0.5 nM of ABC for 16 h at 37 ºC before imaging. Experiments were performed in triplicate with qualitatively identical results. Scale bars, 100 µm. B: Size exclusion chromatography of ABC(D651A) after integration in MSP5ΔH5-POPC nanodiscs. The main peak fraction indicated in green was used for cryo-EM. C: Negative-stain electron micrograph of the peak fraction indicated in A, showing predominantly holotoxin pores. Scale bar, 100 nm.

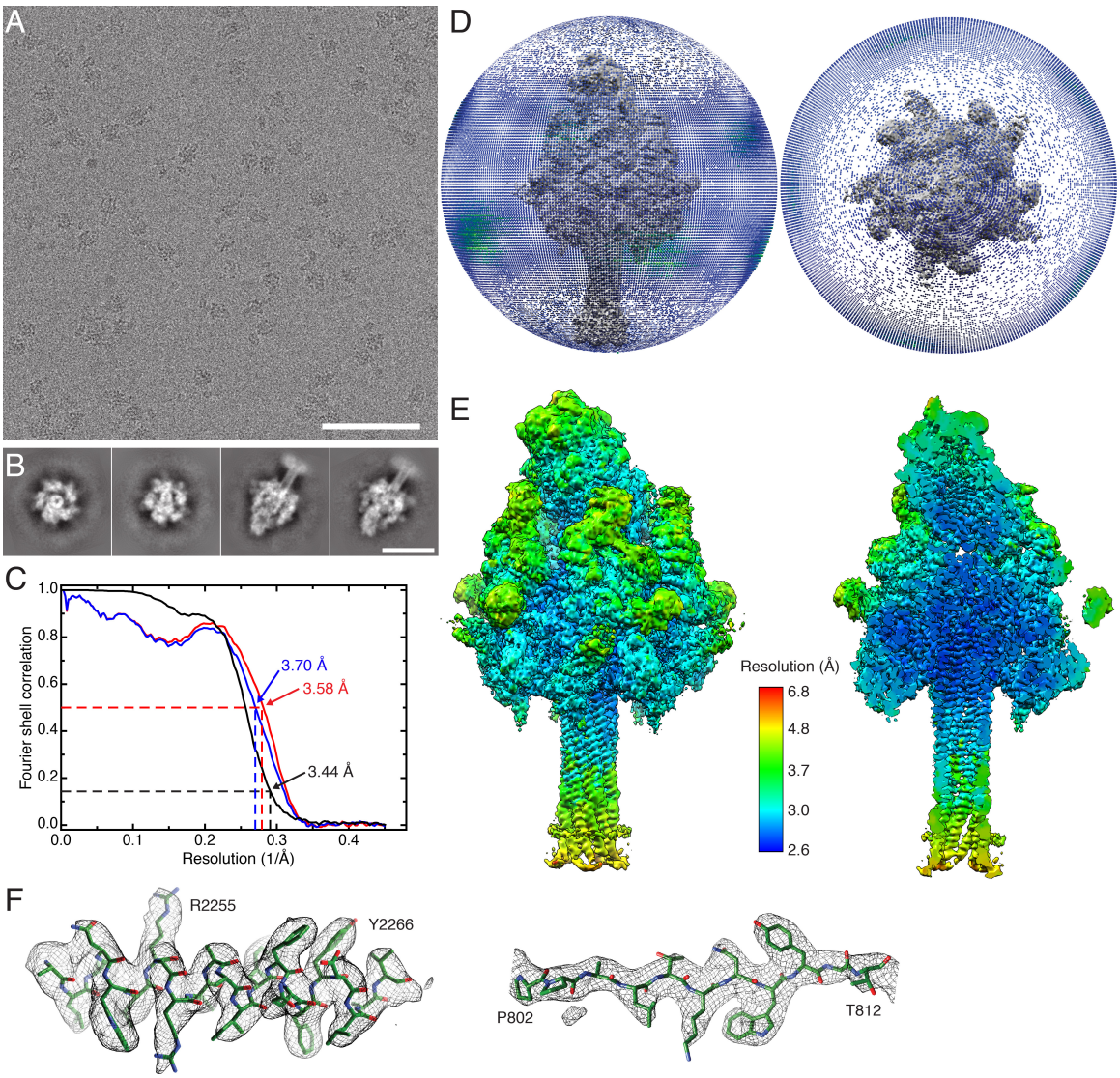

Fig. S2. Cryo-EM of ABC(D651A) in a nanodisc.

A: Representative electron micrograph of vitrified ABC(D651A) at 2.1 µm defocus and 100 $e^-/Å^2$ total dose acquired with a Falcon 3 direct electron detector. Scale bar, 100 nm. B: Representative 2D class averages. Top views (left two images) and side views (right two images) are shown. Scale bar, 20 nm. C: Fourier shell correlation (FSC) of the obtained cryo-EM map (black curve). The 0.143 criterion indicates an average resolution of 3.4 Å. The red and blue curves show the map-to-model FSCs of two independently refined half maps. D: Angular distribution plots of the final round of refinement in side view and top view. Each stick represents a projection view. The size and color of sticks (blue-to-green) is proportional to the number of particles. E: Local resolution estimation of the cryo-EM density map, side view (left) and section (right), colored according to local resolution. F: Superimpositions of representative areas of the cryo-EM density maps and the models, shown for an α-helical part in TcA (left) and a β-strand in TcB (right).

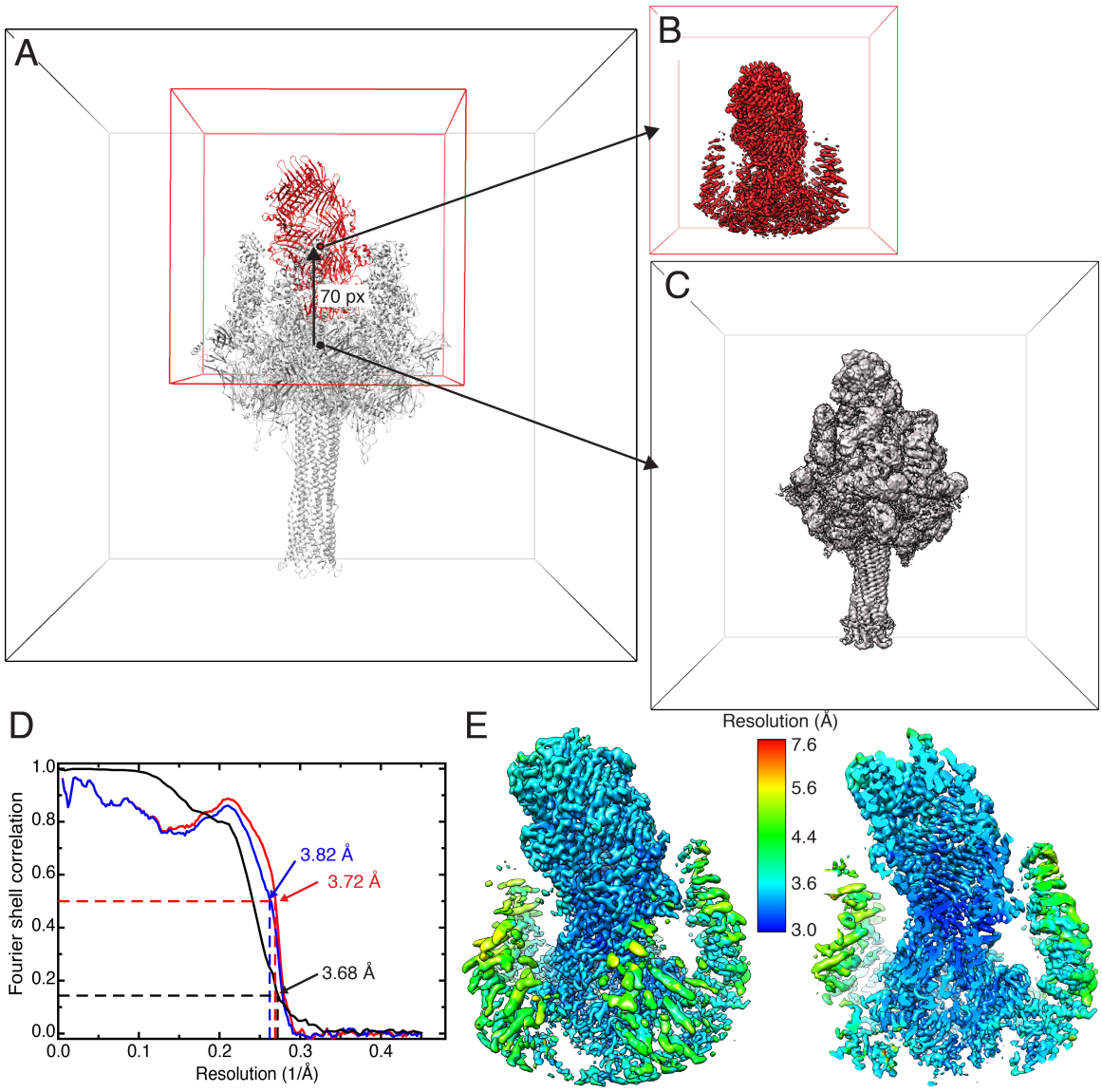

Fig. S3. Shift of the particle box center from the center of ABC(D651A) to the center of TcB-TcC.

A: Scheme of shift of box center from the center of the ABC(D651A) holotoxin (black dot) to the center of TcB-TcC (red dot) by 70 pixels (corresponds to 78 Å). The box was re-scaled from 384 pixels to 200 pixels. The model of the holotoxin is shown in the box for comparison, with TcA in gray and TcB-TcC in red. B,C: Cryo-EM maps of the final refinement of the shifted reconstruction (B, red) and the original reconstruction of the full ABC(D651A) holotoxin (C, gray). The particle boxes of the maps are also depicted. D: Fourier shell correlation (FSC) of the obtained cryo-EM map (black curve). The 0.143 criterion indicates an average resolution of 3.7 Å. The red and blue curves show the map-to-model FSCs of two independently refined half maps. E: Local resolution estimation of the cryo-EM map, side view (left) and section (right), colored according to local resolution.

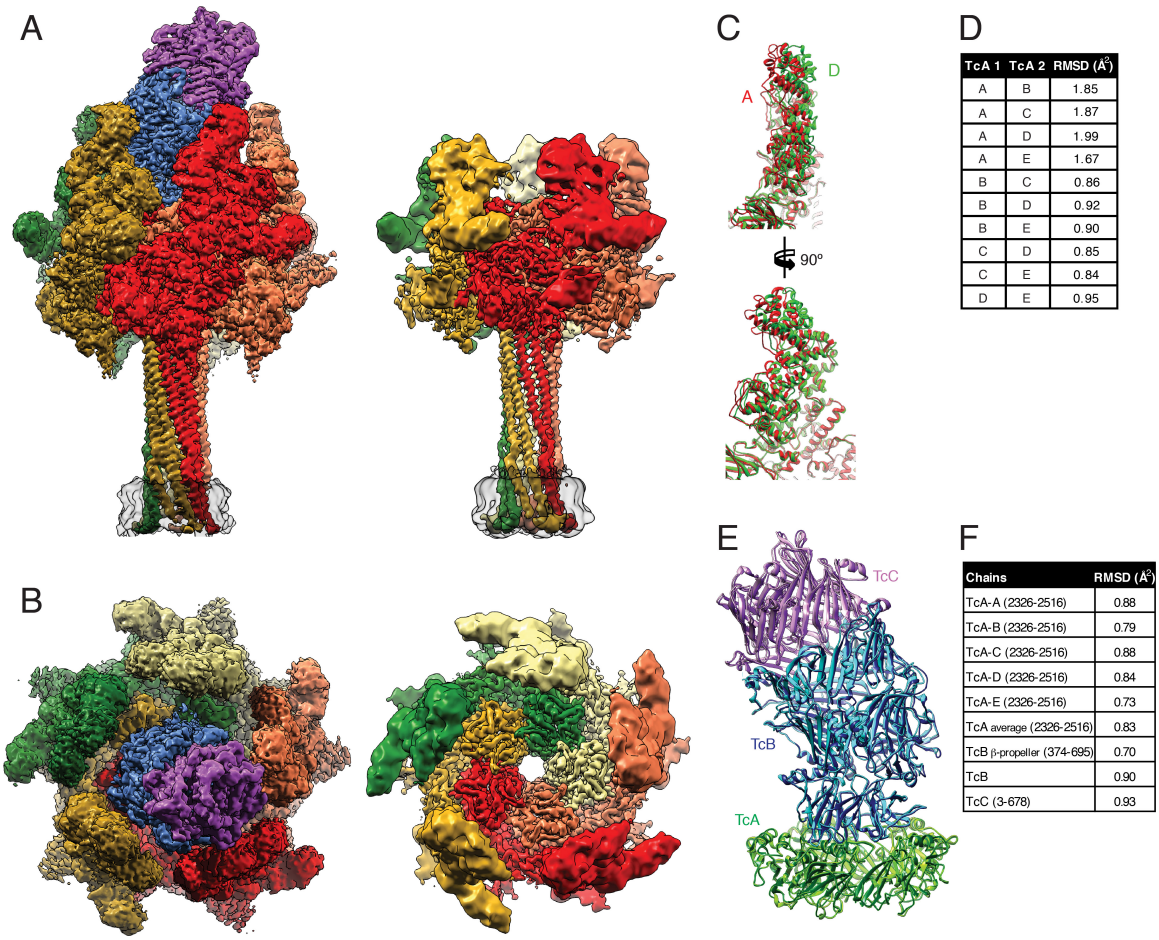

TcA 1	TcA 2	RMSD (Å)
A	B	1.85
A	C	1.87
A	D	1.99
A	E	1.67
B	C	0.86
B	D	0.92
B	E	0.90
C	D	0.85
C	E	0.84
D	E	0.95

Chains	RMSD (Å)
TcA-A (2326-2516)	0.88
TcA-B (2326-2516)	0.79
TcA-C (2326-2516)	0.88
TcA-D (2326-2516)	0.84
TcA-E (2326-2516)	0.73
TcA average (2326-2516)	0.83
TcB β-propeller (374-695)	0.70
TcB	0.90
TcC (3-678)	0.93

Fig. S4. Comparison of cryo-EM maps of ABC(D651A) and TcA.

A: Side view of the density maps of ABC(D651A) and TcA (EMDB 4068) embedded in lipid nanodiscs. B: Top views of the maps in panel A. The individual subunits and the nanodiscs are colored like in Fig. 1A. C: Overlay of the upper parts (residues 290 – 980) of TcA protomers A (red) and D (green). Front view (top) and side view (bottom) show a gradual increase of displacement with further distance to the center of TcA. D: Backbone RMSDs between the individual TcA chains, calculated in Chimera. E: Overlay of models of the TcB-TcC and TcA (residues 2327-2516) of the prepore of ABC(D651A) (pdb ID 6H6F, light colors) with the respective model of the pore of ABC(D651A) (dark colors). The TcB-binding domains of TcA were aligned on each other. F: Backbone RMSDs of the individual TcA chains, all TcA chains combined, the β-propeller domain of TcB, TcB and TcC between the prepore and pore form of ABC(D651A). RMSD values were calculated in Chimera

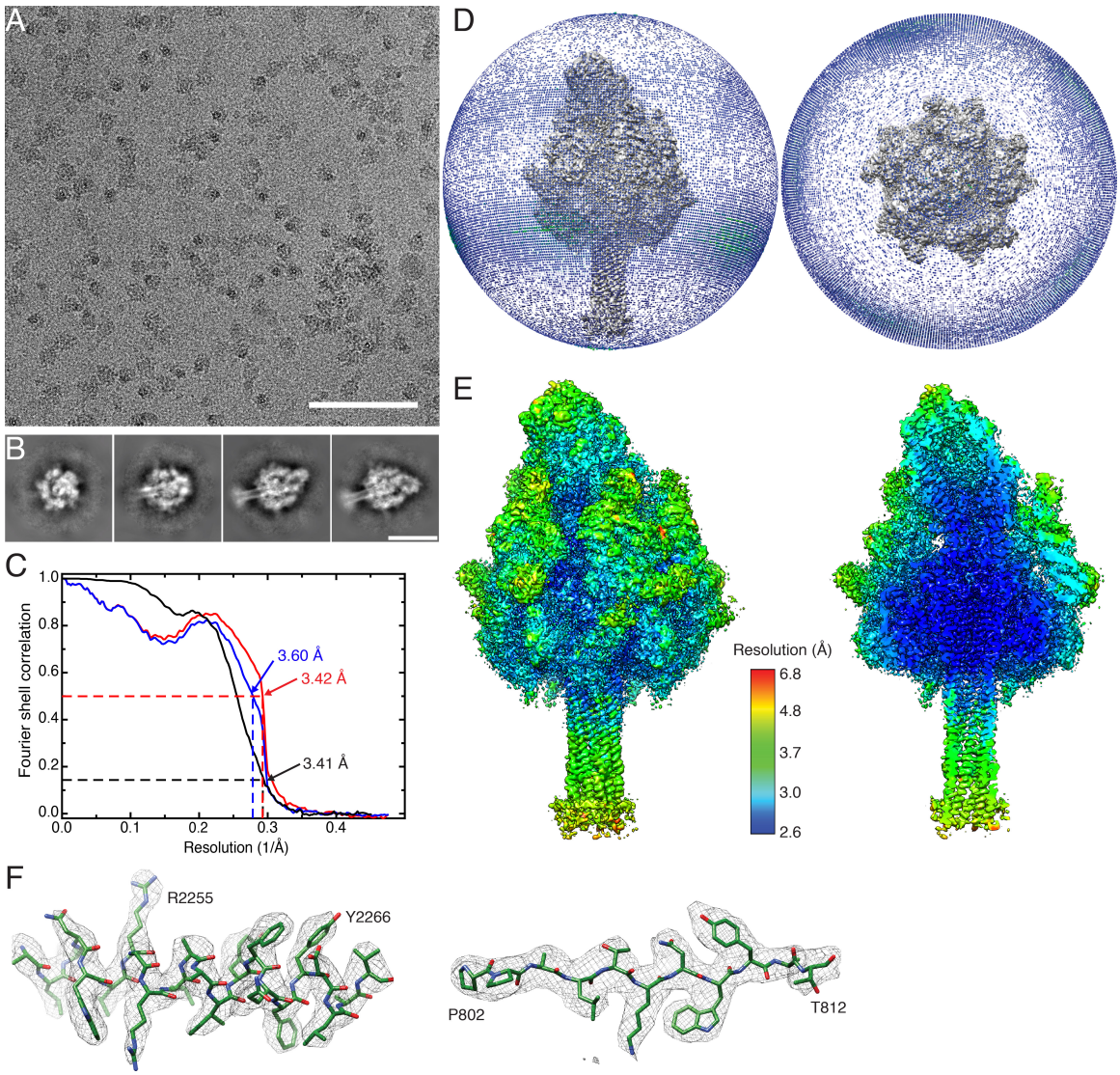

Fig. S5. Cryo-EM of ABC(WT) in a nanodisc.

A: Representative electron micrograph of vitrified ABC(WT) at 2.0 µm defocus and 63 $e^-/Å^2$ total dose acquired with a K2 direct electron detector. Scale bar, 100 nm. B: Representative 2D class averages. Top and tilted views (left two images) and side views (right two images) are shown. Scale bar, 20 nm. C: Fourier shell correlation (FSC) of the obtained cryo-EM map (black curve). The 0.143 criterion indicates an average resolution of 3.4 Å. The red and blue curves show the map-to-model FSCs of two independently refined half maps. D: Angular distribution plots of the final round of refinement in side view and top view. Each stick represents a projection view. The size and color of sticks (blue-to-green) is proportional to the number of particles. E: Local resolution estimation of the cryo-EM map, side view (left) and section (right), colored according to local resolution. F: Superimpositions of representative areas of the cryo-EM density maps and the models, shown for an α-helical part in TcA (left) and a β-strand in TcB (right).

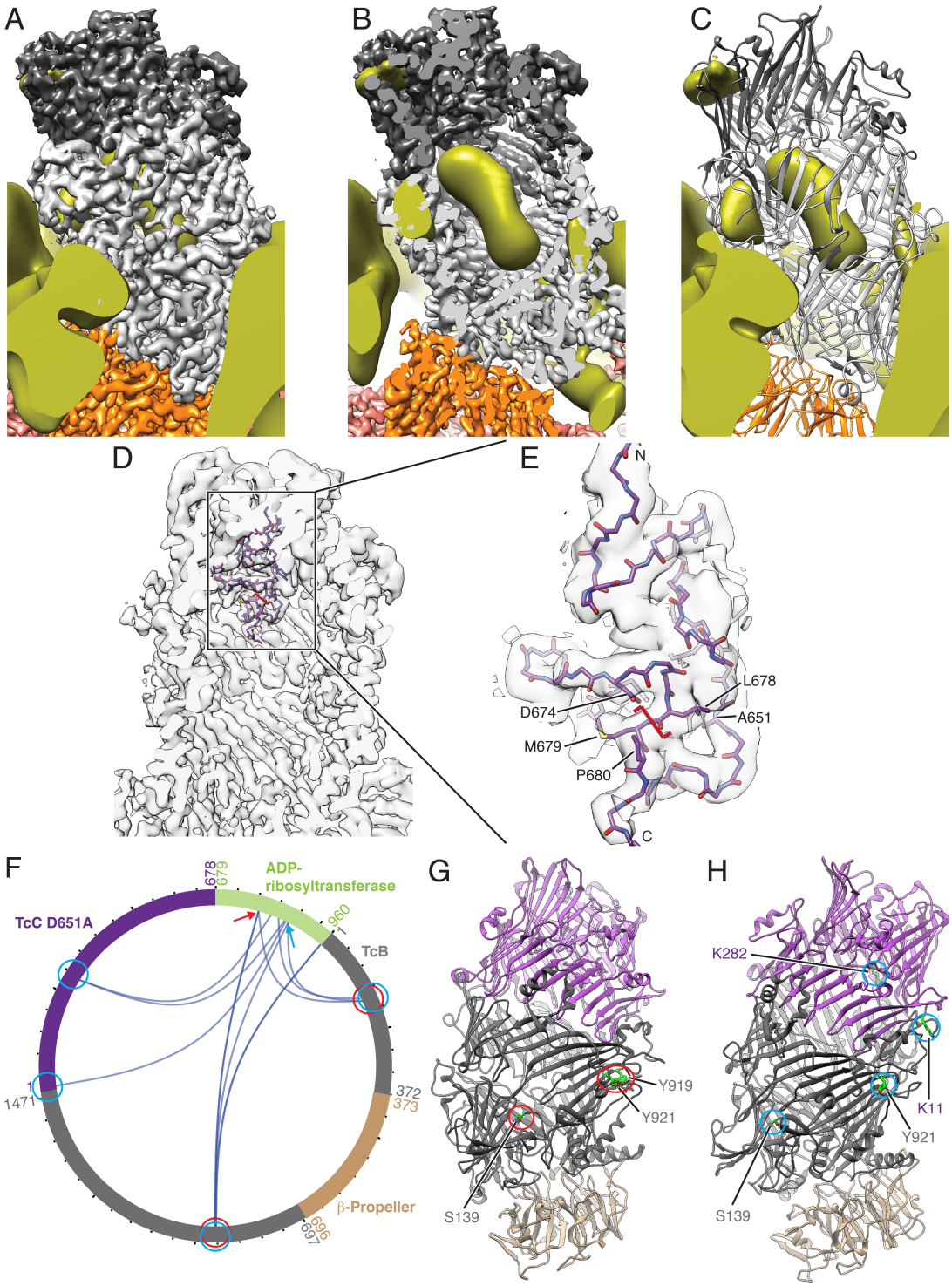

Fig. S6. Variability analysis of the TcB-TcC cocoon, visualization of the aspartyl protease domain of TcC and XL-MS analysis of ABC(D651A) with encapsulated, non-cleaved toxic enzyme.

A-C: 3D variability analysis of the ABC(D651A) structure. The 3D average and variance map were created in SPHIRE **(6)** with the input images filtered to 25 Å. The 3D variance map is shown in gold. A,B: Overlay of the cryo-EM density map of ABC(D651A) (colored in pale red, orange, light

gray and dark gray according to TcA, TcB β-propeller, TcB cocoon and TcC, respectively) and 3D variance map in side view (A) and section (B). C: Model of TcB-TcC with the 3D variance map (gold). Note the highest variance in the center of the cocoon and at the upper domains of TcA. D: Position of the aspartyl autoprotease domain (residues 618 – 678 of TcC) with the attached N-terminus of the toxic enzyme (residues 679 – 683 of TcC) in the TcB-TcC cocoon. The model is overlaid with the cryo-EM map obtained by shifting the center of reconstruction (Fig. S3). The cleavage site is indicated (red bracket). E: Detailed view of panel D. The protein is cleaved between L678 and M679. The residues forming the aspartyl autoprotease cleavage site (D674 and A651, which is D651 in WT) and the conserved P680 are indicated. F: Visualization of crosslinks (dark blue curves) in TcB-TcC-D651A between the TcB-TcC cocoon (gray and violet, β-propeller in sand) and the ADP-ribosyltransferase (green). Two individual positions (K785 and K853, K856, K863 of TcC) and their crosslinks to the TcB-TcC cocoon are indicated with red and blue arrows and circles, respectively. All crosslinks with a score of 50 and higher are shown. The plot was created using xVis **(19)**. A complete list of all crosslinks is shown in Table S3. G,H: The TcB-TcC cocoon with all amino acids that crosslink with K785 indicated and highlighted with red circles (G) and crosslinks with K853, K856, K863 indicated and highlighted with blue circles (H).

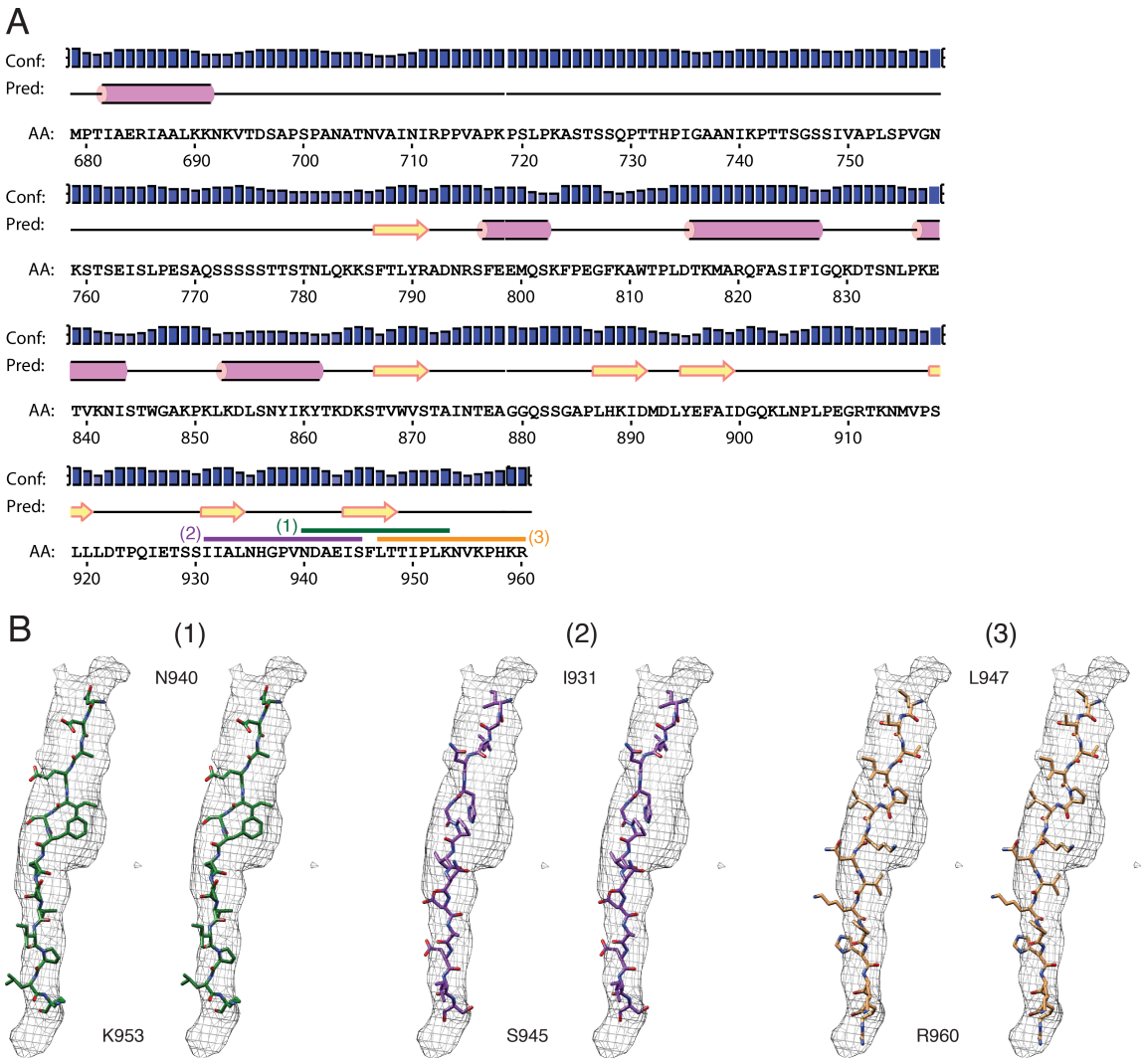

Fig. S7: Comparison of different models close to the C-terminus of the toxic enzyme in the density in the narrow passage of TcB.

A: Secondary structure prediction of the ADP-ribosyltransferase of TccC3, obtained by PSIPRED (56). Predicted α-helices are shown as purple cylinders, β-strands are shown as yellow arrows. The positions of modeled peptides in B are shown as green, purple and orange bars. Residue numbering starts with the first residue after the cleavage site of TcC (M679). Conf: confidence, Pred: prediction, AA: residue. B: Stereo views of three atomic models of possible peptides close to the C-terminus of the ADP-ribosyltransferase in the cryo-EM density (shown as mesh representation) in the narrow passage of TcB. N940 – K953 (green) fits best, with the bulky density in the center occupied by F946.

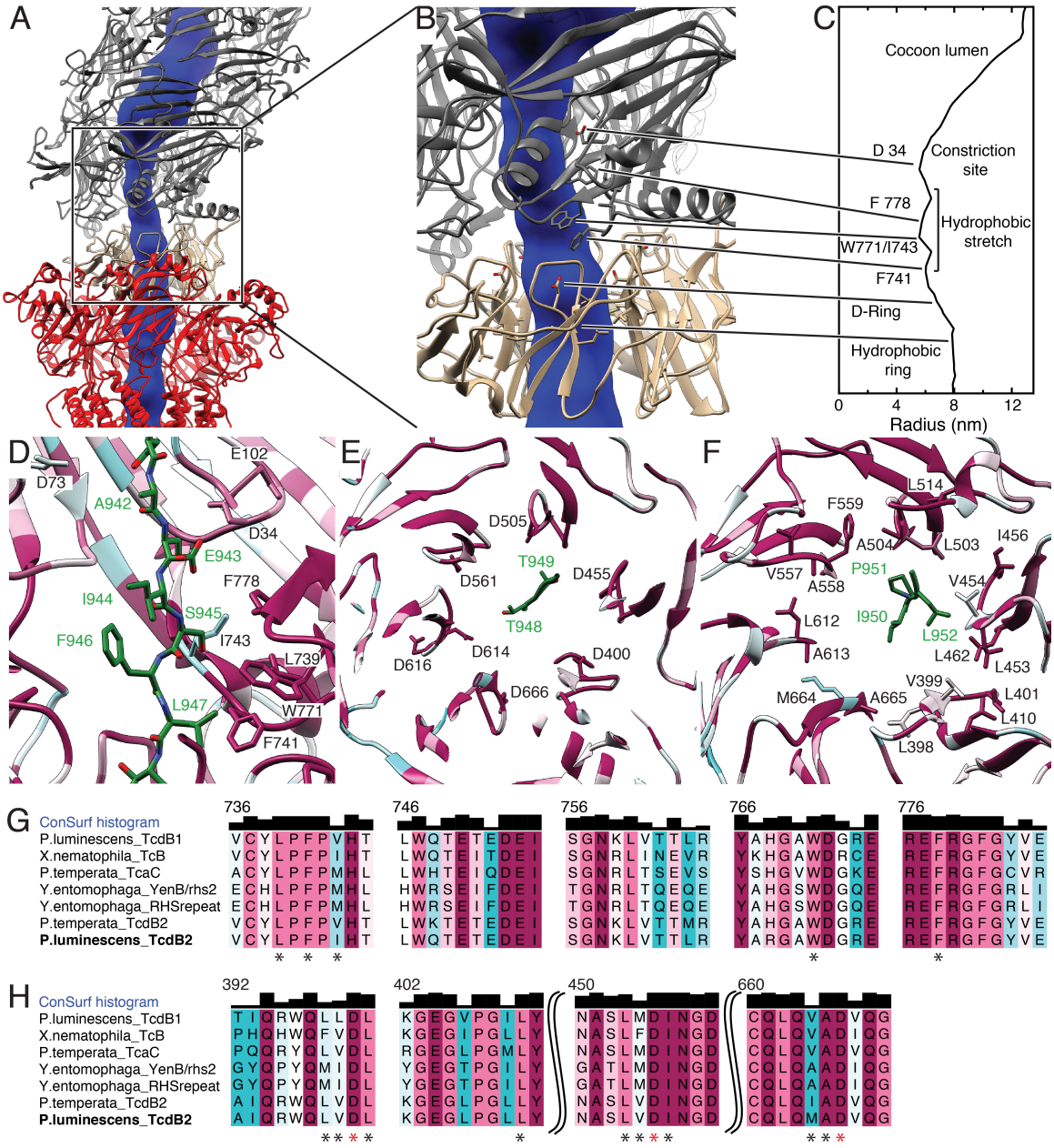

Fig. S8: Analysis of translocation channel of TcB and conservation plot of residues.

A: The central translocation channel of TcB, spanning from the cocoon (gray) through the TcB β-propeller (sand) to TcA (red). The channel lumen obtained by ChExVis (49) is shown in blue. B: Section of panel a, showing constrictions in the TcB β-propeller and cocoon. D34 in the constriction site and residues of the hydrophobic stretch, the D-ring and the hydrophobic ring (see Fig. 6) are shown. C: Plot of inner radius of the TcB channel. Residues and motifs forming constrictions are indicated. D-F: The constriction site and the hydrophobic stretch (D), the negatively charged ring (E) and the hydrophobic ring (F) with mapped sequence conservation ranging from minimum (cyan) to maximum (magenta). The translocating ADP-ribosyltransferase is depicted in green. Views and highlighted residues are the same like in Fig. 6C-E. G: Sequence alignment of the hydrophobic stretch of TcB. Residues shown in panel D are indicated (*). H: Sequence alignment of selected regions of the D-ring and the hydrophobic ring. Residues shown in panels E and F are indicated by red and black asterisks, respectively.

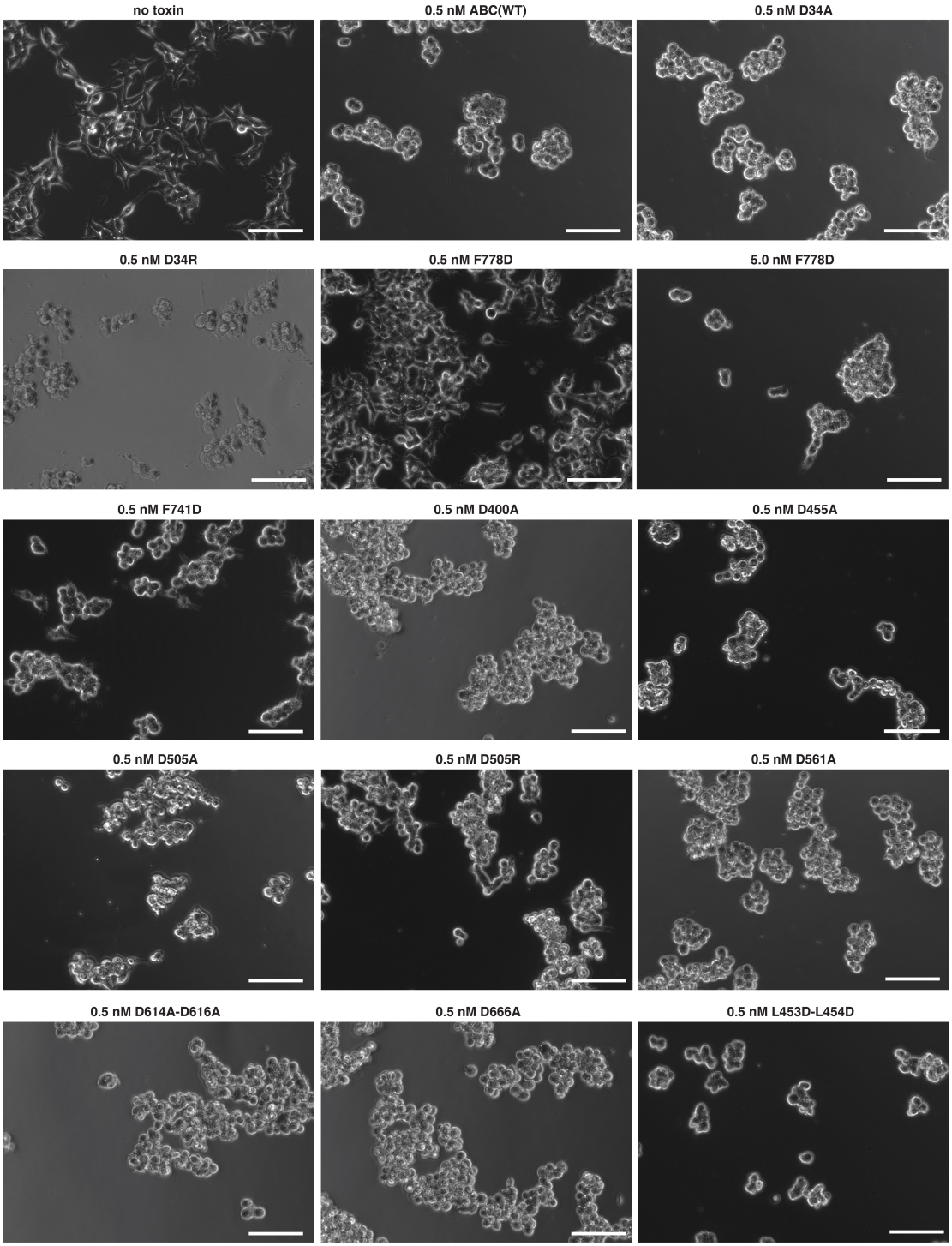

Fig. S9. Comparison of toxicity of TcB variants.

Intoxication of HEK 293T cells with holotoxins formed by TcA(WT) and the indicated TcB-TcC variants. Intoxicated cells round up and detach from the surface. 2×10^4 cells in DMEM/F12 medium were incubated with 0.5 nM or 5.0 nM of ABC for 16 h at 37 ºC before imaging. Experiments were performed in duplicates with qualitatively identical results. Scale bars, 100 μm.

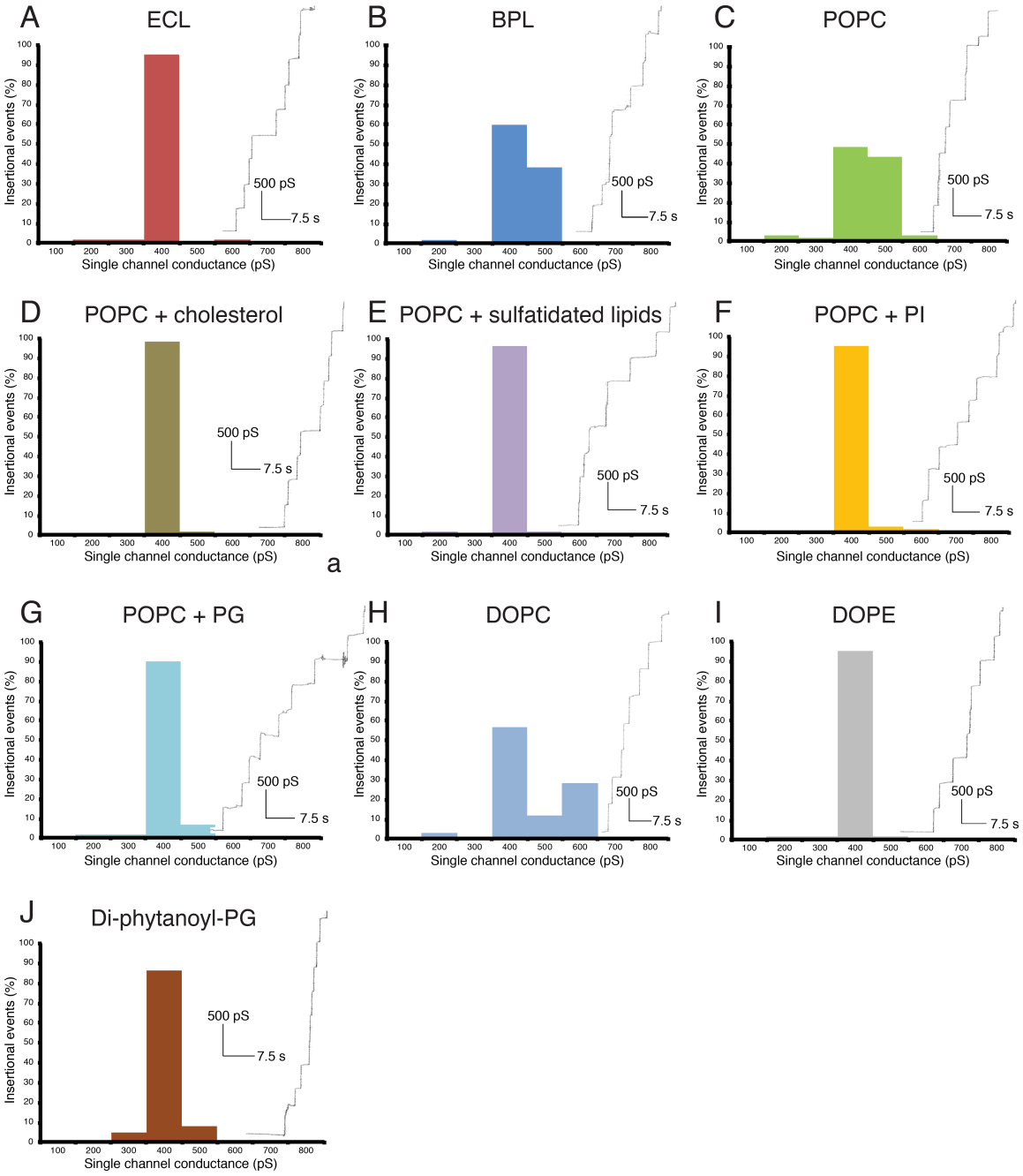

Fig. S10: Single channel conductance of TcA in different lipids.

All histograms were constructed from the data of 60 pore insertional events for each condition. For each experiment, an exemplary recording of the single-channel current versus time is shown next to the histogram. A: TcA and *E. coli* polar lipid extract (ECL). B: TcA and brain polar lipid extract (BPL). C: TcA and POPC. D: TcA and POPC with 20% cholesterol. E: TcA and POPC with 20% sulfatide. F: TcA and POPC with 20% liver phosphatidylinositol (PI). G: TcA and POPC with 20% phosphatidylglycerol (PG). H: TcA and di-oleoyl-phosphatidylcholine (DOPC). I: TcA and di-oleoyl-phosphatidylethanolamine (DOPE). J: TcA and di-phytanoyl-phosphatidylglycerol.

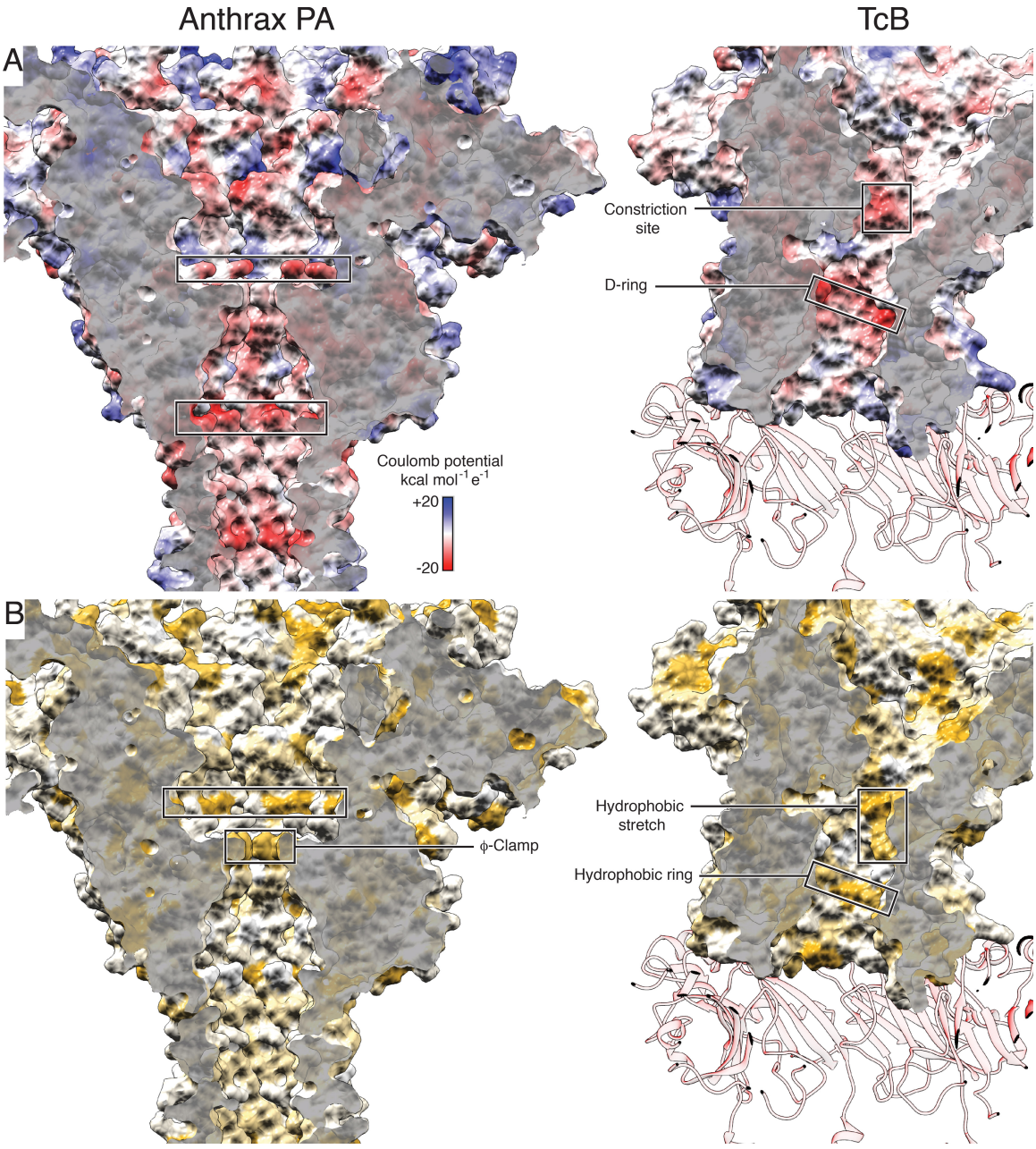

Fig. S11: Comparison of the Coulomb potentials and surface hydrophobicities of the translocation channels of anthrax protective antigen (PA) with the narrow passage of TcB.

A: Surface representation of anthrax PA (left) and TcB (right), colored according to the Coulomb potential (kcal mol^{-1} e^{-1}) at pH 7.0. The interacting parts of TcA at the bottom are shown as transparent ribbon representation. The negatively charged regions of both structures close to the channel constrictions are highlighted in boxes. Translocation direction is from top to bottom. B: The same view as in panel A, colored according to hydrophobicity. Hydrophobic regions are colored ochre, non-hydrophobic regions are colored white. Hydrophobic regions inside the channels are highlighted in boxes.

Legends for Supplementary Movies

Movie S1 (separate file):
Cryo-EM density map of the ABC(D651A) pore with the fitted atomic model. Representative areas of the cryo-EM density in TcA and TcB-TcC are shown.

Movie S2 (separate file):
Morph between TcA-A (red) and the other four TcA chains, visualizing the structural changes in the upper part of the □-helical shell in comparison to the rest of the molecule.

Movie S3 (separate file):
Move through vertical slices along the central axis of ABC(D651A) and ABC(WT) pore. TcA, TcB and TcC are shown as ribbon representations. The nanodisc is shown in transparent gray. Additional density not corresponding to the atomic models is filtered to 10 Å and shown in dark gray.

Movie S4 (separate file):
Cryo-EM density map of the ABC(D651A) pore after shifting the center of reconstruction. The atomic model of TcB-TcC (blue and purple, respectively) is fitted into the map. In the second part, the movie zooms in and focuses on the aspartyl protease domain of TcC.

Movie S5 (separate file):
Cryo-EM density map inside the narrow passage of TcB with the different C-terminal polypeptides of the ADP-ribosyltransferase fitted into the density (Fig. S7B).

Movie S6 (separate file):
Morph of the cryo-EM density of the ABC(D651A) prepore (EMDB 0150) to the density of the ABC(D651A) pore in a nanodisc. The morph between the densities is followed by a morph between the states using the atomic models of the proteins, showing the prepore-to-pore transition on the level of the holotoxin and the opening of the translocation channel in the membrane. The outer shell, the linker and the transmembrane channel of TcA are shown in red, black and yellow, respectively. TcB is shown in blue, and TcC is shown in purple.

Supplementary Tables

Table S1. Cryo-EM data collection, refinement and validation statistics for ABC(D651A) and ABC(WT).

	TcdA1-TcdB2-TccC3-D651A, pore form in nanodiscs (EMDB-10312) (PDB 6SUE)	TcdA1-TcdB2-TccC3 wt, pore form in nanodiscs (EMDB-10313) (PDB 6SUF)
Data collection and processing		
Camera	Falcon III	K2
Magnification	59,000	130,000
Voltage (kV)	300	300
Exposure time (s)	1.5	15
Total electron exposure (e–/Å^2)	100	61
Defocus range (μm)	1.2 – 2.6	1.4 – 2.6
Pixel size (Å)	1.11	1.05
Symmetry imposed	C1	C1
Initial particle images (no.)	619,594	269,142
Final particle images (no.)	337,823	64,806
Map resolution (Å) FSC threshold	3.4 0.143	3.4 0.143
Map resolution range (Å)	2.6-6.8	2.6 – 6.8
Map sharpening *B* factor (Å^2)	-78.09	-61.28
Refinement		
Initial model used (PDB code)	4O9X, 5LKH, 5LKI	ABC(D651A)
Model resolution (Å) FSC threshold	3.5 0.5	3.4 0.5
Model composition Non-hydrogen atoms Protein residues Ligands	 108,272 13,628	 108,122 13,607
Mean B factors (Å^2) Protein	 107.3	 63.3
R.m.s. deviations Bond lengths (Å) Bond angles (°)	 0.021 1.68	 0.021 1.77
Validation MolProbity score EMRinger score Clashscore Favored rotamers (%) Poor rotamers (%) Rosetta FSC_{work}/FSC_{free}	 0.89 2.68 1.12 99.57 0.01 0.6464/0.6355	 1.68 2.93 1.51 99.66 0.00 0.6783/0.6595
Ramachandran plot Favored (%) Allowed (%) Disallowed (%)	 97.69 99.72 0.28	 97.38 99.74 0.26

Table S2. Crosslinks of TcB-TcC(WT) that were detected by mass spectrometry. Crosslinks between the TcB-TcC cocoon and the ADP-ribosyltransferase (HVR) are highlighted in red, and crosslinks between TcB-TcC and HVR with a score of at least 50 that are shown in Fig. 5A are indicated.

Protein1	Protein2	AbsPos1	AbsPos2	Score	false discovery rate	Score ≥ 50
TcB	TcB	136	1395	18	0.005	
TcB	TcB	482	520	30	0	
TcB	TcB	637	1302	96	0	
TcB	TcB	859	866	104	0	
TcB	TcB	872	807	28	0.006	
TcB	TcB	919	637	48	0	
TcB	TcB	921	1395	80	0	
TcB	TcB	946	846	101	0	
TcB	TcB	1175	402	13	0.011	
TcB	TcB	1177	311	48	0	
TcB	TcB	1177	319	95	0	
TcB	TcB	1177	328	69	0	
TcB	TcC	1177	160	81	0	
TcB	TcB	1278	637	96	0	
TcB	TcB	1278	647	94	0	
TcB	TcB	1278	1302	92	0	
TcB	TcB	1278	1304	117	0	
TcB	TcB	1280	1304	13	0	
TcB	TcB	1304	1450	13	0.011	
TcB	TcC	1304	655	11	0.004	
TcB	TcB	1417	1422	99	0	
TcB	TcB	1439	1477	24	0.006	
TcB	TcC	1439	9	98	0	
TcB	TcC	1439	11	96	0	
TcC	TcB	41	1395	23	0	
TcC	TcC	124	142	63	0	
TcC	TcB	308	1422	111	0	
TcC	TcB	308	1425	84	0	
TcC	TcB	308	1428	106	0	
TcC	TcC	308	296	86	0	
TcC	TcC	308	297	53	0.004	
TcC	TcC	308	315	88	0	
TcC	TcC	308	316	104	0	
TcC	TcB	309	1422	101	0	
TcC	TcC	309	316	49	0	
TcC	TcC	313	308	101	0	
TcC	TcC	313	348	22	0.006	
TcC	TcC	315	348	33	0	
TcC	TcC	478	484	35	0	
TcC	TcC	481	484	81	0	
TcC	TcC	481	493	116	0	
TcC	TcC	484	142	45	0	
TcC	TcC	484	511	33	0.006	

TcC	TcC	622	282	38	0.007	
TcC	TcC	625	560	79	0	
TcC	TcC	625	618	85	0	
TcC	TcC	625	619	126	0	
TcB	HVR	136	817	44	0.007	
TcB	HVR	136	837	47	0	
TcB	HVR	762	817	24	0.006	
TcB	HVR	762	837	25	0.006	
TcB	HVR	762	849	31	0.006	
TcB	HVR	762	853	28	0.006	
TcB	HVR	919	785	101	0	x
TcB	HVR	921	785	126	0	x
TcB	HVR	1473	882	12	0	
TcC	HVR	622	956	27	0	
TcC	HVR	625	679	58	0	x
TcC	HVR	625	785	105	0	x
HVR	TcC	679	493	14	0	
HVR	TcB	690	762	22	0	
HVR	TcB	690	763	34	0.007	
HVR	TcB	690	766	30	0.006	
HVR	TcC	690	273	24	0	
HVR	TcC	690	282	125	0	x
HVR	TcC	690	625	147	0	x
HVR	TcB	785	136	42	0.007	
HVR	TcB	785	139	112	0	x
HVR	TcB	785	762	24	0.006	
HVR	TcB	785	1439	7	0.004	
HVR	TcB	849	136	39	0	
HVR	TcB	853	139	76	0	x
HVR	TcB	863	132	23	0	
HVR	TcB	863	139	108	0	x
HVR	TcB	863	762	24	0.006	
HVR	TcB	959	132	20	0	
HVR	HVR	679	785	127	0	
HVR	HVR	679	790	100	0	
HVR	HVR	679	803	118	0	
HVR	HVR	679	809	112	0	
HVR	HVR	679	816	99	0	
HVR	HVR	679	817	122	0	
HVR	HVR	679	837	84	0	
HVR	HVR	679	839	119	0	
HVR	HVR	679	849	120	0	
HVR	HVR	679	853	112	0	
HVR	HVR	679	856	54	0	
HVR	HVR	679	860	111	0	
HVR	HVR	679	865	98	0	
HVR	HVR	679	903	92	0	
HVR	HVR	690	679	125	0	

HVR	HVR	690	681	127	0	
HVR	HVR	690	785	153	0	
HVR	HVR	690	790	137	0	
HVR	HVR	690	802	124	0	
HVR	HVR	690	803	113	0	
HVR	HVR	690	809	114	0	
HVR	HVR	690	816	119	0	
HVR	HVR	690	830	117	0	
HVR	HVR	690	837	133	0	
HVR	HVR	690	839	144	0	
HVR	HVR	690	849	129	0	
HVR	HVR	690	853	125	0	
HVR	HVR	690	858	102	0	
HVR	HVR	690	860	126	0	
HVR	HVR	690	863	143	0	
HVR	HVR	690	865	103	0	
HVR	HVR	690	882	47	0	
HVR	HVR	690	903	115	0	
HVR	HVR	690	959	131	0	
HVR	HVR	785	796	33	0	
HVR	HVR	785	802	126	0	
HVR	HVR	785	803	126	0	
HVR	HVR	785	809	115	0	
HVR	HVR	785	817	134	0	
HVR	HVR	785	830	126	0	
HVR	HVR	785	837	119	0	
HVR	HVR	785	849	127	0	
HVR	HVR	785	853	139	0	
HVR	HVR	785	865	113	0	
HVR	HVR	786	817	126	0	
HVR	HVR	786	853	110	0	
HVR	HVR	788	837	99	0	
HVR	HVR	788	853	22	0	
HVR	HVR	788	865	91	0	
HVR	HVR	790	803	122	0	
HVR	HVR	802	784	33	0	
HVR	HVR	802	830	35	0	
HVR	HVR	802	853	50	0	
HVR	HVR	803	718	83	0	
HVR	HVR	803	830	113	0	
HVR	HVR	809	830	115	0	
HVR	HVR	809	865	92	0	
HVR	HVR	809	883	67	0	
HVR	HVR	816	741	40	0	
HVR	HVR	816	784	67	0	
HVR	HVR	816	803	112	0	
HVR	HVR	816	830	114	0	
HVR	HVR	816	865	72	0	

HVR	HVR	817	741	94	0	
HVR	HVR	817	803	142	0	
HVR	HVR	817	830	128	0	
HVR	HVR	817	832	109	0	
HVR	HVR	830	784	107	0	
HVR	HVR	833	853	84	0	
HVR	HVR	837	803	119	0	
HVR	HVR	837	809	120	0	
HVR	HVR	837	816	105	0	
HVR	HVR	837	817	122	0	
HVR	HVR	837	860	110	0	
HVR	HVR	837	862	117	0	
HVR	HVR	837	871	77	0	
HVR	HVR	837	872	33	0	
HVR	HVR	839	803	108	0	
HVR	HVR	839	817	96	0	
HVR	HVR	844	865	8	0	
HVR	HVR	849	796	26	0	
HVR	HVR	849	802	104	0	
HVR	HVR	849	803	116	0	
HVR	HVR	849	809	116	0	
HVR	HVR	849	816	75	0	
HVR	HVR	849	817	36	0.007	
HVR	HVR	849	830	121	0	
HVR	HVR	849	837	125	0	
HVR	HVR	849	839	126	0	
HVR	HVR	849	860	117	0	
HVR	HVR	849	865	76	0	
HVR	HVR	853	803	84	0	
HVR	HVR	853	809	121	0	
HVR	HVR	853	812	12	0.011	
HVR	HVR	853	816	135	0	
HVR	HVR	853	817	74	0	
HVR	HVR	853	830	118	0	
HVR	HVR	853	837	102	0	
HVR	HVR	853	839	27	0	
HVR	HVR	853	849	140	0	
HVR	HVR	853	858	72	0	
HVR	HVR	853	865	110	0	
HVR	HVR	856	718	91	0	
HVR	HVR	856	785	108	0	
HVR	HVR	856	803	120	0	
HVR	HVR	856	849	124	0	
HVR	HVR	858	785	117	0	
HVR	HVR	858	803	102	0	
HVR	HVR	858	837	115	0	
HVR	HVR	858	849	112	0	
HVR	HVR	860	803	130	0	

HVR	HVR	860	809	121	0	
HVR	HVR	860	812	111	0	
HVR	HVR	860	816	121	0	
HVR	HVR	860	817	135	0	
HVR	HVR	860	833	60	0	
HVR	HVR	862	785	50	0	
HVR	HVR	862	803	124	0	
HVR	HVR	863	679	91	0	
HVR	HVR	863	718	43	0	
HVR	HVR	863	785	121	0	
HVR	HVR	863	802	100	0	
HVR	HVR	863	803	107	0	
HVR	HVR	863	809	105	0	
HVR	HVR	863	837	117	0	
HVR	HVR	863	839	117	0	
HVR	HVR	863	849	135	0	
HVR	HVR	863	853	147	0	
HVR	HVR	863	856	51	0	
HVR	HVR	863	858	127	0	
HVR	HVR	863	882	29	0	
HVR	HVR	863	903	114	0	
HVR	HVR	863	956	143	0	
HVR	HVR	956	785	113	0	
HVR	HVR	956	803	27	0	
HVR	HVR	956	816	47	0	
HVR	HVR	956	837	57	0	
HVR	HVR	956	849	48	0	
HVR	HVR	956	860	39	0	
HVR	HVR	959	853	86	0	

Table S3. Crosslinks of TcB-TcC(D651A) that were detected by mass spectrometry. Crosslinks between the TcB-TcC cocoon and the ADP-ribosyltransferase (HVR) are highlighted in red, and crosslinks between TcB-TcC and HVR with a score of at least 50 that are shown in Fig. S6F are indicated.

Protein1	Protein2	AbsPos1	AbsPos2	Score	false discovery rate	Score ≥ 50
TcB	TcB	1278	1278	133	0.000	
TcC	TcC	313	308	132	0.000	
TcB	TcB	534	525	130	0.000	
TcB	TcB	1439	1470	122	0.000	
TcB	TcB	534	474	117	0.000	
TcB	TcB	921	1395	112	0.000	
TcB	TcB	520	521	111	0.000	
TcB	TcB	1278	1304	109	0.000	
TcB	TcB	1177	319	108	0.000	
TcB	TcB	1442	1470	107	0.000	
TcB	TcB	1439	1473	105	0.000	
TcB	TcB	859	866	102	0.000	
TcC	TcC	618	144	102	0.000	
TcB	TcB	946	840	100	0.000	
TcC	TcB	7	1477	99	0.000	
TcC	TcB	308	1428	99	0.000	
TcC	TcC	142	156	99	0.000	
TcC	TcB	9	970	97	0.000	
TcB	TcB	1278	521	94	0.000	
TcB	TcB	1177	320	92	0.000	
TcC	TcB	308	1431	92	0.000	
TcB	TcC	1439	11	91	0.000	
TcB	TcC	1278	144	91	0.000	
TcC	TcB	308	1425	90	0.000	
TcB	TcB	1278	268	90	0.000	
TcB	TcB	402	521	90	0.000	
TcB	TcB	946	846	89	0.000	
TcB	TcB	1278	496	87	0.000	
TcC	TcC	481	484	85	0.000	
TcB	TcC	1177	160	84	0.000	
TcB	TcC	1278	562	84	0.000	
TcB	TcC	1439	9	82	0.000	
TcB	TcB	411	520	82	0.000	
TcB	TcB	1278	883	82	0.000	
TcB	TcB	952	846	82	0.000	
TcC	TcC	484	144	81	0.000	
TcC	TcB	484	1278	81	0.000	
TcC	TcC	504	625	80	0.000	
TcB	TcB	1278	272	79	0.000	
TcB	TcB	536	521	76	0.000	
TcB	TcB	1278	1302	76	0.000	
TcC	TcC	618	625	75	0.000	
TcB	TcB	866	840	75	0.000	

TcB	TcB	534	476	74	0.000	
TcB	TcB	1177	311	71	0.000	
TcC	TcC	309	316	70	0.000	
TcB	TcC	1278	142	68	0.000	
TcC	TcC	625	504	61	0.000	
TcB	TcB	866	880	56	0.000	
TcC	TcC	625	618	56	0.000	
TcB	TcB	1278	1267	54	0.000	
TcB	TcB	1177	331	51	0.000	
TcB	TcB	1178	320	47	0.000	
TcC	TcC	625	619	45	0.000	
TcB	TcB	921	1278	44	0.000	
TcC	TcB	493	1278	37	0.000	
TcB	TcB	921	846	37	0.000	
TcC	TcB	484	1280	36	0.000	
TcC	TcB	309	1422	36	0.000	
TcC	TcB	11	966	35	0.000	
TcC	TcC	12	504	34	0.000	
TcC	TcC	496	484	32	0.000	
TcB	TcB	866	846	31	0.000	
TcB	TcB	949	846	31	0.000	
TcB	TcB	916	883	30	0.001	
TcC	TcC	313	348	30	0.001	
TcC	TcC	308	301	28	0.001	
TcC	TcC	625	484	28	0.001	
TcC	TcC	481	493	28	0.001	
TcC	TcB	11	970	26	0.001	
TcB	TcB	766	320	25	0.002	
TcC	TcC	623	484	21	0.003	
TcB	TcB	476	883	20	0.003	
TcB	TcC	268	11	20	0.003	
TcC	TcB	313	1422	19	0.004	
TcC	TcC	308	313	19	0.004	
TcB	TcB	534	482	18	0.005	
TcB	TcB	520	902	13	0.013	
TcC	TcC	484	496	13	0.013	
TcC	TcC	504	484	13	0.013	
TcB	TcC	1177	323	13	0.013	
TcB	TcC	1280	484	12	0.014	
TcB	TcB	1177	419	12	0.014	
TcB	TcB	520	1133	11	0.018	
TcB	TcB	1177	158	11	0.018	
TcC	TcB	313	1278	10	0.020	
TcB	TcB	1280	272	10	0.020	
TcB	TcB	1177	991	9	0.023	
TcC	TcB	671	846	8	0.028	
TcB	TcC	859	160	7	0.033	
TcC	TcB	308	482	7	0.033	

TcB	TcB	1425	520	7	0.033	
TcB	TcC	1278	277	6	0.037	
TcB	TcB	534	872	6	0.037	
TcB	TcB	345	414	5	0.044	
TcB	TcB	1214	1051	5	0.044	
HVR	TcB	863	921	106	0.000	x
HVR	TcB	785	139	86	0.000	x
HVR	TcC	856	11	80	0.000	x
HVR	TcC	853	282	79	0.000	x
HVR	TcB	959	919	76	0.000	x
HVR	TcC	817	282	66	0.000	x
HVR	TcB	959	921	53	0.000	x
HVR	TcB	863	139	50	0.000	x
HVR	TcB	785	136	38	0.000	
HVR	TcB	853	136	35	0.000	
HVR	TcB	853	139	30	0.001	
HVR	TcB	809	1296	27	0.001	
HVR	TcC	959	410	26	0.001	
HVR	TcB	849	136	25	0.002	
HVR	TcB	785	143	24	0.002	
HVR	TcB	691	1425	23	0.003	
HVR	TcB	863	136	23	0.003	
HVR	TcB	863	132	22	0.003	
HVR	TcB	786	272	22	0.003	
HVR	TcC	690	277	20	0.003	
HVR	TcB	837	143	20	0.003	
HVR	TcB	959	143	14	0.012	
HVR	TcC	837	7	10	0.020	
HVR	TcB	853	1286	10	0.020	
HVR	TcB	839	272	9	0.023	
TcB	HVR	919	785	104	0.000	x
TcB	HVR	921	785	103	0.000	x
TcB	HVR	132	837	53	0.000	x
TcB	HVR	136	837	42	0.000	
TcB	HVR	921	817	38	0.000	
TcC	HVR	625	959	35	0.000	
TcB	HVR	139	817	24	0.002	
TcC	HVR	147	860	19	0.004	
TcB	HVR	139	837	13	0.013	
TcB	HVR	520	754	12	0.014	
TcB	HVR	1392	809	9	0.023	
TcB	HVR	1280	817	5	0.044	
HVR	HVR	690	863	177	0.000	
HVR	HVR	690	837	175	0.000	
HVR	HVR	863	849	173	0.000	
HVR	HVR	863	785	173	0.000	
HVR	HVR	690	853	166	0.000	
HVR	HVR	863	853	164	0.000	

HVR	HVR	837	862	162	0.000	
HVR	HVR	849	837	162	0.000	
HVR	HVR	956	862	161	0.000	
HVR	HVR	956	860	161	0.000	
HVR	HVR	863	856	161	0.000	
HVR	HVR	837	860	161	0.000	
HVR	HVR	860	817	161	0.000	
HVR	HVR	863	959	160	0.000	
HVR	HVR	690	785	156	0.000	
HVR	HVR	690	959	156	0.000	
HVR	HVR	863	816	156	0.000	
HVR	HVR	785	853	156	0.000	
HVR	HVR	849	817	155	0.000	
HVR	HVR	690	816	153	0.000	
HVR	HVR	853	849	150	0.000	
HVR	HVR	863	956	149	0.000	
HVR	HVR	959	862	148	0.000	
HVR	HVR	863	830	148	0.000	
HVR	HVR	959	785	148	0.000	
HVR	HVR	785	839	146	0.000	
HVR	HVR	785	860	146	0.000	
HVR	HVR	790	837	146	0.000	
HVR	HVR	959	853	143	0.000	
HVR	HVR	959	849	143	0.000	
HVR	HVR	690	862	142	0.000	
HVR	HVR	817	849	142	0.000	
HVR	HVR	959	839	142	0.000	
HVR	HVR	853	816	142	0.000	
HVR	HVR	849	839	141	0.000	
HVR	HVR	863	839	141	0.000	
HVR	HVR	849	862	138	0.000	
HVR	HVR	858	849	138	0.000	
HVR	HVR	863	858	137	0.000	
HVR	HVR	863	803	136	0.000	
HVR	HVR	853	817	136	0.000	
HVR	HVR	853	837	136	0.000	
HVR	HVR	785	849	133	0.000	
HVR	HVR	786	837	132	0.000	
HVR	HVR	817	833	132	0.000	
HVR	HVR	785	830	132	0.000	
HVR	HVR	690	839	131	0.000	
HVR	HVR	849	809	130	0.000	
HVR	HVR	785	809	129	0.000	
HVR	HVR	853	809	129	0.000	
HVR	HVR	690	803	128	0.000	
HVR	HVR	837	809	127	0.000	
HVR	HVR	959	830	126	0.000	
HVR	HVR	860	833	126	0.000	

HVR	HVR	849	803	125	0.000	
HVR	HVR	785	817	124	0.000	
HVR	HVR	860	803	124	0.000	
HVR	HVR	690	833	123	0.000	
HVR	HVR	690	817	123	0.000	
HVR	HVR	959	837	123	0.000	
HVR	HVR	860	865	123	0.000	
HVR	HVR	860	841	123	0.000	
HVR	HVR	849	833	123	0.000	
HVR	HVR	849	860	122	0.000	
HVR	HVR	862	865	122	0.000	
HVR	HVR	837	817	122	0.000	
HVR	HVR	959	809	121	0.000	
HVR	HVR	959	803	121	0.000	
HVR	HVR	785	833	121	0.000	
HVR	HVR	790	803	121	0.000	
HVR	HVR	860	812	121	0.000	
HVR	HVR	817	803	121	0.000	
HVR	HVR	785	803	120	0.000	
HVR	HVR	785	832	120	0.000	
HVR	HVR	856	809	119	0.000	
HVR	HVR	853	803	119	0.000	
HVR	HVR	690	849	118	0.000	
HVR	HVR	833	959	118	0.000	
HVR	HVR	785	865	118	0.000	
HVR	HVR	853	839	118	0.000	
HVR	HVR	839	817	0	0.000	
HVR	HVR	837	803	116	0.000	
HVR	HVR	785	862	116	0.000	
HVR	HVR	863	833	115	0.000	
HVR	HVR	837	812	110	0.000	
HVR	HVR	860	809	109	0.000	
HVR	HVR	785	816	108	0.000	
HVR	HVR	824	817	108	0.000	
HVR	HVR	858	830	107	0.000	
HVR	HVR	817	832	107	0.000	
HVR	HVR	856	803	107	0.000	
HVR	HVR	817	830	107	0.000	
HVR	HVR	849	867	105	0.000	
HVR	HVR	790	741	105	0.000	
HVR	HVR	817	865	105	0.000	
HVR	HVR	862	803	105	0.000	
HVR	HVR	837	816	104	0.000	
HVR	HVR	853	833	103	0.000	
HVR	HVR	785	845	102	0.000	
HVR	HVR	837	883	102	0.000	
HVR	HVR	858	785	102	0.000	
HVR	HVR	830	802	101	0.000	

HVR	HVR	849	830	98	0.000	
HVR	HVR	862	809	98	0.000	
HVR	HVR	786	809	98	0.000	
HVR	HVR	803	833	97	0.000	
HVR	HVR	863	809	96	0.000	
HVR	HVR	839	803	95	0.000	
HVR	HVR	690	809	94	0.000	
HVR	HVR	785	903	94	0.000	
HVR	HVR	849	903	94	0.000	
HVR	HVR	690	860	94	0.000	
HVR	HVR	785	802	93	0.000	
HVR	HVR	830	903	91	0.000	
HVR	HVR	903	769	91	0.000	
HVR	HVR	802	809	91	0.000	
HVR	HVR	803	784	91	0.000	
HVR	HVR	959	865	89	0.000	
HVR	HVR	839	865	88	0.000	
HVR	HVR	863	788	88	0.000	
HVR	HVR	841	833	88	0.000	
HVR	HVR	903	778	87	0.000	
HVR	HVR	959	802	87	0.000	
HVR	HVR	809	833	87	0.000	
HVR	HVR	816	903	87	0.000	
HVR	HVR	956	817	86	0.000	
HVR	HVR	785	837	86	0.000	
HVR	HVR	959	841	86	0.000	
HVR	HVR	837	895	83	0.000	
HVR	HVR	856	849	83	0.000	
HVR	HVR	830	732	83	0.000	
HVR	HVR	956	816	82	0.000	
HVR	HVR	861	809	80	0.000	
HVR	HVR	830	803	80	0.000	
HVR	HVR	839	851	77	0.000	
HVR	HVR	956	785	77	0.000	
HVR	HVR	863	837	76	0.000	
HVR	HVR	788	817	75	0.000	
HVR	HVR	883	784	74	0.000	
HVR	HVR	785	858	73	0.000	
HVR	HVR	833	784	71	0.000	
HVR	HVR	959	889	71	0.000	
HVR	HVR	853	741	67	0.000	
HVR	HVR	903	784	66	0.000	
HVR	HVR	956	833	61	0.000	
HVR	HVR	903	867	61	0.000	
HVR	HVR	785	812	61	0.000	
HVR	HVR	809	732	61	0.000	
HVR	HVR	786	903	60	0.000	
HVR	HVR	863	844	59	0.000	

HVR	HVR	956	803	57	0.000	
HVR	HVR	690	903	57	0.000	
HVR	HVR	959	817	56	0.000	
HVR	HVR	863	817	53	0.000	
HVR	HVR	863	778	52	0.000	
HVR	HVR	809	741	52	0.000	
HVR	HVR	860	851	51	0.000	
HVR	HVR	817	725	51	0.000	
HVR	HVR	863	790	50	0.000	
HVR	HVR	817	741	50	0.000	
HVR	HVR	959	816	48	0.000	
HVR	HVR	849	895	48	0.000	
HVR	HVR	788	809	48	0.000	
HVR	HVR	956	790	47	0.000	
HVR	HVR	956	853	46	0.000	
HVR	HVR	839	784	45	0.000	
HVR	HVR	839	741	43	0.000	
HVR	HVR	853	785	42	0.000	
HVR	HVR	871	784	41	0.000	
HVR	HVR	959	790	40	0.000	
HVR	HVR	837	785	39	0.000	
HVR	HVR	959	784	38	0.000	
HVR	HVR	849	816	38	0.000	
HVR	HVR	865	780	37	0.000	
HVR	HVR	959	693	33	0.000	
HVR	HVR	690	784	31	0.000	
HVR	HVR	690	693	31	0.000	
HVR	HVR	849	741	31	0.000	
HVR	HVR	959	860	28	0.001	
HVR	HVR	803	865	28	0.001	
HVR	HVR	844	784	28	0.001	
HVR	HVR	839	718	27	0.001	
HVR	HVR	777	865	26	0.001	
HVR	HVR	790	784	26	0.001	
HVR	HVR	863	693	25	0.002	
HVR	HVR	956	809	24	0.002	
HVR	HVR	790	817	24	0.002	
HVR	HVR	817	883	23	0.003	
HVR	HVR	959	788	21	0.003	
HVR	HVR	690	741	21	0.003	
HVR	HVR	817	796	21	0.003	
HVR	HVR	837	844	21	0.003	
HVR	HVR	817	790	20	0.003	
HVR	HVR	839	913	20	0.003	
HVR	HVR	959	858	20	0.003	
HVR	HVR	858	809	17	0.007	
HVR	HVR	790	809	16	0.008	
HVR	HVR	959	780	15	0.009	

SI References

1. Gatsogiannis C, et al. (2013) A syringe-like injection mechanism in Photorhabdus luminescens toxins. *Nature* 495(7442):520–523.

2. Gatsogiannis C, et al. (2016) Membrane insertion of a Tc toxin in near-atomic detail. *Nat Struct Mol Biol* 23(10):884–890.

3. Denisov IG, Grinkova YV, Lazarides AA, Sligar SG (2004) Directed self-assembly of monodisperse phospholipid bilayer Nanodiscs with controlled size. *J Am Chem Soc* 126(11):3477–3487.

4. Zheng SQ, et al. (2017) MotionCor2: anisotropic correction of beam-induced motion for improved cryo-electron microscopy. *Nat Methods* 14(4):331–332.

5. Penczek PA, et al. (2014) CTER-rapid estimation of CTF parameters with error assessment. *Ultramicroscopy* 140:9–19.

6. Moriya T, et al. (2017) High-resolution Single Particle Analysis from Electron Cryo-microscopy Images Using SPHIRE. *J Vis Exp* 2017(123):e55448–e55448.

7. Yang Z, Fang J, Chittuluru J, Asturias FJ, Penczek PA (2012) Iterative stable alignment and clustering of 2D transmission electron microscope images. *Structure* 20(2):237–247.

8. Zhang K, Li M, Sun F (2011) *Gautomatch: an efficient and convenient gpu-based automatic particle selection program*.

9. Wagner T, et al. (2018) SPHIRE-crYOLO: A fast and well-centering automated particle picker for cryo-EM. *bioRxiv* 145:356584.

10. Lopéz-Blanco JR, Chacón P (2013) iMODFIT: efficient and robust flexible fitting based on vibrational analysis in internal coordinates. *J Struct Biol* 184(2):261–270.

11. Emsley P, Lohkamp B, Scott WG, Cowtan K (2010) Features and development of Coot. *Acta Crystallogr D Biol Crystallogr* 66(Pt 4):486–501.

12. Afonine PV, et al. (2018) Real-space refinement in Phenix for cryo-EM and crystallography. doi:10.1101/249607.

13. Kim DE, Chivian D, Baker D (2004) Protein structure prediction and analysis using the Robetta server. *Nucleic Acids Res* 32(Web Server issue):W526–31.

14. DiMaio F, et al. (2015) Atomic-accuracy models from 4.5-Å cryo-electron microscopy data with density-guided iterative local refinement. *Nat Methods* 12(4):361–365.

15. Barad BA, et al. (2015) EMRinger: side chain-directed model and map validation for 3D cryo-electron microscopy. *Nat Methods* 12(10):943–946.

16. Chen VB, et al. (2010) MolProbity: all-atom structure validation for macromolecular crystallography. *Acta Crystallogr D Biol Crystallogr* 66(Pt 1):12–21.

17. Efremov RG, Leitner A, Aebersold R, Raunser S (2015) Architecture and conformational switch mechanism of the ryanodine receptor. *Nature* 517(7532):39–43.

18. Goetze M, et al. (2015) Automated Assignment of MS/MS Cleavable Cross-Links in Protein 3D-Structure Analysis. *J Am Soc Mass Spectrom* 26(1):83–97.

19. Grimm M, Zimniak T, Kahraman A, Herzog F (2015) xVis: a web server for the schematic visualization and interpretation of crosslink-derived spatial restraints. *Nucleic Acids Res* 43(W1):W362–9.

20. Masood TB, Sandhya S, Chandra N, Natarajan V (2015) CHEXVIS: a tool for molecular channel extraction and visualization. *BMC Bioinformatics* 16(1):119.

21. Pettersen EF, et al. (2004) UCSF Chimera--a visualization system for exploratory research and analysis. *J Comput Chem* 25(13):1605–1612.

22. Anandakrishnan R, Aguilar B, Onufriev AV (2012) H++ 3.0: automating pK prediction and the preparation of biomolecular structures for atomistic molecular modeling and simulations. *Nucleic Acids Res* 40(Web Server issue):W537–41.

23. Altschul SF, Gish W, Miller W, Myers EW, Lipman DJ (1990) Basic local alignment search tool. *J Mol Biol* 215(3):403–410.

24. Sievers F, et al. (2011) Fast, scalable generation of high-quality protein multiple sequence alignments using Clustal Omega. *Mol Syst Biol* 7(1):539–539.

25. Ashkenazy H, et al. (2016) ConSurf 2016: an improved methodology to estimate and visualize evolutionary conservation in macromolecules. *Nucleic Acids Res* 44(W1):W344–50.